Large scale dynamics in a turbulent compressible rotor/stator cavity flow at high Reynolds number

C Lachize, G Verhille, P Le Gal

Large scale dynamics in a turbulent compressible rotor/stator cavity flow at high Reynolds number

C. Lachize, G. Verhille, P. Le Gal

Aix Marseille Université, CNRS, Centrale Marseille, IRPHE UMR 7342, 13384, Marseille, France

E-mail: gautier.verhille@irphe.univ-mrs.fr

Abstract. This paper reports an experimental investigation of a turbulent flow confined within a rotor/stator cavity of aspect ratio close to unity at high Reynolds number. The experiments have been driven by changing both the rotation rate of the disk and the thermodynamical properties of the working fluid. This fluid is sulfur hexafluoride (SF_6) whose physical properties are adjusted by imposing the operating temperature and the absolute pressure in the pressurized vessel, especially near the critical point of SF_6 reached for $T_C = 45.58$ °C, $P_C = 37.55$ bar. This original set-up allows to obtain Reynolds numbers as high as $2\ 10^7$ together with compressibility effects as the Mach number can reach 0.5. Pressure measurements reveal that the resulting fully turbulent flow shows both a direct and an inverse cascade as observed in rotating turbulence and in accordance with Kraichnan conjecture for 2D-turbulence. The spectra are however dominated by low-frequency peaks, which are subharmonics of the rotating disk frequency, involving large scale structures at small azimuthal wavenumbers. These modes appear for a Reynolds number around 10^5 and experience a transition at a critical Reynolds number $Re_C \approx 10^6$. Moreover they show an unexpected non linear behavior that we understand with the help of a low dimensional amplitude equations.

Keywords Rotor-stator flows, Large scale dynamics, Compressible turbulence

1. Introduction

For closed cylindrical geometries, laminar flows entrained by rotating disks are commonly assumed to be axisymmetric due to the spatial configuration and boundary condition symmetries. This feature was confirmed by early experimental observations of Escudier (1984) but is obviously particularly restricted to low Reynolds numbers flows before bifurcations and turbulence arise. In particular, one knows that these confined flows can naturally break their axial symmetry leading to stationary or oscillatory behavior. The multiplicity of flow states has motivated many studies, both numerical (Gelfgat et al. 2001, Lopez et al. 2001) and experimental (Stevens et al. 1999, Sørensen et al. 2006) where three dimensional and unsteady regimes were exhibited. However, we may think that increasing the Reynolds number will result in a fully developed turbulent flow where axisymmetry can be restored 'on average' that is without any persistent large scale coherent structures. From a fundamental point of view but also from an industrial point of view, it is of great interest to know if turbulence can sustain these large scale coherent motions and under which circumstances. For instance in turbomachinery, the presence of these large scale coherent structures could drastically modify thermal and momentum transfer predictions, as well as pressure and load distributions. In consequence, it is of capital interest to understand the complex and subtle dynamics that might occur in these systems at low frequency and small wavenumber even at high Reynolds numbers. The rotor-stator cavity flow has then become a popular prototype laboratory flow where physical mechanisms can be deeply analyzed.

Rotor-stator flows possess three relevant governing parameters that define the different hydrodynamics regimes: the height-to-radius aspect ratio ($\gamma = H/R$), the rotational Reynolds number Re and the Mach number Ma (both based on the radius and the angular velocity of the disk). Using these parameters, the literature neglects generally the influence of compressibility and reports classically two different configurations: those with high aspect ratios ($\gamma > 1$) and those corresponding to thin cavities ($\gamma < 1$). In these two cases, if the Reynolds number is not too low (see for instance Schouveiler et al. (1998)), the structure of the basic flow (often referred as the Batchelor flow) consists in one boundary layer attached on each disk: a centripetal Bödewadt layer on the stator and an Ekman layer on the rotor creating a meridional recirculation because of Ekman pumping. Theses layers are separated by a core rotating nearly as a solid body at a rate equal to half the disk rotation rate. This core is surrounded by a cylindrical boundary layer attached to the sidewall of the cylindrical container. Note that if the description of the Batchelor flow ignores the finite geometry of the system and the presence of the cylindrical sidewall, it is usually admitted and experimentally observed that rotor-stator flows with stationary sidewall keep this arrangement. However reverse or separated boundary layers can in fact be observed in more complex geometries such as those with inward throughflow (Poncet et al. 2005) or contra-rotating end-walls or rotating sidewalls (Lopez 1998). Although we cannot

achieve a detailed description of the velocity fields in our set-up, we will keep this classical description as it has also been observed in previous rotor/stator experiments using similar aspect ratios, see for instance Sørensen et al. (2006).

2. State of the art

2.1. Thin cylindrical rotor/stator cavities

For very thin cavities ($\gamma \approx 0.1$), Gelfgat (2015) has observed that the flow becomes unstable for Reynolds numbers $Re \sim O(10^4)$ and with large azimuthal wave numbers m. These spiral patterns with around 20 arms and their different transitions have been the subject of many experimental studies in the 90's (see for instance Schouveiler et al. (1998), Schouveiler et al. (2001) and Gauthier et al. (2002), or the review by Launder et al. (2010)). They find their origin in the crossflow instability of the Bödewadt layer on the stator and were recently simulated by Lopez et al. (2009). The report of a small number of azimuthal structures is however scarce. It was described in the experimental visualizations of Czarny et al. (2002) who reported the occurrence of three dimensional unsteady large scale vortices for $\gamma = 0.126$ and 0.195 and Re ranged from $3.7\ 10^4$ to $2.24\ 10^5$. For both lowest Re and lowest γ, no coherent structure was detectable whereas increasing Re to $1.12\ 10^5$ activates the development of a 2-lobe pattern which rotates at approximately half the rate of the rotating disk. When Re and γ were increased, the flow was prone to produce organized large scale tripolar vortices or pentagonal structures. Finally, the estimation of their velocity enables to locate these structures in the core. These dynamics have been reproduced by Poncet et al. (2009) with both experimental visualizations and numerical simulations where the Reynolds number ranges up to $Re = 2.15\ 10^6$. They have noticed that the generation of vortical structures is highly sensitive to the time history of the flow and depends on the experimental procedure (except for mode with $m = 2$ and 3 which are indifferently observed). Moreover, the selected azimuthal wave number decreases when the rotation rate increases and the presence of an inner central hub (annulus cavity) prevents the formation of such low azimuthal wavenumber structures.

2.2. Tall cylindrical rotor/stator cavities

In tall geometries ($\gamma > 1$), Ekman pumping is responsible for streamline deformations and induces stagnation points along the axis of rotation, driving the generation of steady axisymmetric recirculation bubbles. Escudier's experimental observations allow to identify and characterize the flow topology over a wide range of (Re,γ) respectively between [1000 ; 4000] (i.e. for laminar flows) and [1 ; 3.5]. He mapped out a transition-diagram, accounting for the existence of one or multiple steady bubbles as well as unsteady hydrodynamic structures. He associated these recirculations to vortex breakdown that occurs at a critical Reynolds number equal to approximately 2600. With the same goals, Lopez (1990) then Gelfgat et al. (1996) have treated this problem with

axisymmetric numerical formulations keeping the same flow parameters than Escudier using respectively direct numerical simulations and numerical linear stability analysis. They have concluded that vortex breakdown does not result directly from instabilities but originates from continuous variations of meridional flow when the Reynolds number is increased. In the early 2000's, Gelfgat et al. (2001) have provided a numerical linear marginal stability of rotor-stator cavity flows for the same range of Re. For γ between 1.63 and 2.76, an axisymmetric mode is found to be the dominant unstable mode, bringing an explanation for the axisymmetric vortex breakdown, whereas out of this range, non-axisymmetric modes with azimuthal wavenumbers $m = 1, 2, 3$ and 4 can arise. The authors have particularly noticed that mode $m = 2$ is dominant for $\gamma < 1.63$ and $m = 3$ or $m = 4$ are prominent for $\gamma > 2.76$. These results have been reinforced by Marques & Lopez (2001) using three dimensional direct numerical simulations. In particular, these authors have observed that disturbances are more significant at the singular junction between the stator and sidewall boundary layers which may indicate that the instability is linked to wall effects. This analysis is corroborated by the calculations of Barbosa (2002), who has performed direct numerical simulations for $\gamma = 1$ and 1.5 and Re in the range $[2400 - 7100]$ (laminar flows). In what concern non-linear regimes, Barbosa (2002) has demonstrated that the linearly dominant modes $m = 2$ and $m = 3$ can feed multiples stable modes $m = 2n$ and $m = 3n$. Besides, these two linearly unstable modes coexist and compete: the most unstable one will damp the other one because their kinetic energies are spatially localized at the same place (near the corner between the stator and the sidewall, as described by Marques & Lopez (2001)). At the same time, computational resources allowed to study the flow destabilization mechanisms. One of the most relevant contributions has been provided by Sotiropoulos & Ventikos (2001) with direct numerical simulations for $\gamma = 1.75$ and 2, and $Re = 1850$ (steady regime) and 7000 (well within the unsteady regime). It appears that disturbances organize themselves in azimuthal modes, involving an asymmetric separation of the sidewall boundary layer in the stator vicinity. The characterization of the cylindrical wall boundary layer has led them to establish that this unsteadiness is generated by a centrifugal-like instability. In the case of a rotating cylindrical wall, these sidewall instabilities have been described some years before in the experiments of Hart & Kittelman (1996). These results were furthermore detailed by the numerical simulations of Lopez & Marques (2010) where backward tilted diagonal rolls destabilize the sidewall boundary layer and sustain inertial waves in the rotating interior flow leading to complex spatiotemporal dynamics. In the same spirit *i.e.* when the cylindrical fluid cavity experiences a global rotation with a differentially rotating lid, low azimuthal wave number instabilities are known to destabilize inner shear layers. Impressive visualizations associated to numerical simulations have been published by Lopez et al. (2002). Three-dimensional non axisymmetric states and their associated complex non linear dynamics were further described in great details in Blackburn & Lopez (2002) and Lopez (2006) for respectively $\gamma = 2.5$ and 1.72. These numerical simulations show in particular that the coexistence of multi axisymmetric and non axisymmetric

modes complicates a lot the prediction of the flow (at least for the considered moderate Reynolds numbers). Indeed, several time scales originate from the competing modal structures and lead to modulated rotating waves whose dynamics depends on initial conditions.

Following these numerical simulations, Sørensen et al. (2006) confirm experimentally for the first time the presence of non-axisymmetric modes with small azimuthal wave numbers between $m = 0$ and $m = 5$. They described accurately by Laser Doppler Anemometry the presence of frequency peaks in the velocity spectra and by Particle Image Velocimetry the spatial structures of the different modes. Because of the possibility to change the height of their laboratory apparatus, they were also able to detail the instability thresholds as a function of the aspect ratio γ and of the Reynolds number Re. These experimental results were completed later by a dual experiment/numerical simulation study of the axisymmetry breaking of the flow in rotating lid driven cavities of larger aspect ratio ($3.3 < \gamma < 5.5$) (Sørensen et al. 2009). Note finally the recent article by Lopez (2012) that confirms the existence of supercritical Hopf bifurcations of low azimuthal wave number modes in these tall geometries, arising from the modulated rotating waves that result from three-dimensional instability of time periodic axisymmetric flows as seen before at intermediate γ (Blackburn & Lopez 2002, Lopez 2006). Our present experimental study can be seen as the pursuit of these two last experimental works of Sørensen et al. (2006) and Sørensen et al. (2009) but where the Reynolds number is not restricted to the vicinity of the instability thresholds (around a few thousands) but can reach much higher values, when developed turbulence invades the whole flow.

2.3. Inertial waves and rotating turbulence

Considering sufficiently rapidly rotating flows, when viscous effects are negligible, external excitations can also sustain inertial travelling waves into the solid body rotation region if their angular frequencies, in the rotating frame, are less than twice the fluid rotation rate. Jacques et al. (2002) performed 2D-axisymmetric numerical simulations in a rotor/stator configuration with $\gamma = 0.125$ in the transitional and turbulent regimes. They especially detailed results for $Re = 3\ 10^5$ and $Re = 10^6$ and underlined the presence of inertial waves for fast enough rotation rates ($Re > 10^5$) which are characterized by large amplitudes and low frequencies within the solid body rotating core. In their opinion, such modes are excited by large scales structures coming out of the turbulent stator boundary layer and propagating up to the rotor through the solid body rotation region. Lopez & Marques (2014) have investigated numerically for Reynolds numbers up to $Re = 10^6$ and for $\gamma = 2$, the stability and robustness of inertial modes in rotating cylinders when these are subjected to sidewall axial oscillations with periodic time-forcing. Their studies show that the propagation angle and axial wavenumbers of these waves only depend on the external forcing frequencies and found that the vortices emanating from the corners are responsible for these waves generation.

However with an axisymmetric forcing mechanism, azimuthal waves $m \neq 0$ are quickly damped. Recently, Gutierrez-Castillo & Lopez (2015) have carried out three dimensional simulations involving the sidewall instability of a rapidly rotating cylinder split at mid-height and an extensive characterization of axisymmetric different states is done for a wide range of γ and Rossby number. It appears that the basic state loses stability through diverse ways involving sidewall boundary layer breathing causing inertial waves to propagate in the core of the flow. When their cavity is axially extended ($\gamma > 1$), large amplitude subharmonics are discernible, leading to the complex superposition of many inertial waves propagating at different angles.

These inertial waves might play also an important role on the energy transfer in rotating turbulence. The strength of the rotation is quantified in this case by the Rossby number $Ro = u/L\Omega_f$ where Ω_f is the fluid rotation rate, u a typical velocity and L a characteristic length. For small Rossby number, the flow tends to be invariant along the direction of the axis of rotation. Thus, rotating turbulence is expected to share some common properties with 2D turbulence. Kraichnan (1967) predicts that two cascades coexist. The first one is an inverse cascade of energy towards the large scales with a velocity power spectrum $\propto k^{-5/3}$ (where k is the magnitude of the wavenumber). The second is a direct cascade of enstrophy towards the small scales and is associated with a velocity power spectrum $\propto k^{-3}$. Baroud et al. (2003) observed for the first time the direct cascade of enstrophy in rotating turbulence. One can notice that this enstrophy cascade stops at the Zeeman scale ℓ_z defined by $u_{\ell_z}/\ell_z\Omega_f = 1$ (*i.e.* when the Coriolis force become smaller than the inertial term). Then for smaller scales, the flow isotropy is recovered. Since 2010, more and more studies are devoted to the inverse cascade of energy and the eventual role of inertial waves in this transfer. Lamriben et al. (2011) studied the decay of turbulence generated by the displacement of a grid in a rotating cubic tank. They observed the apparition of three peaks in the velocity spectrum associated to three inertial modes. This experiment shows the existence of inertial waves in rotating turbulence but does not give any answer on their role in the inverse cascade. To tackle this point, Yarom & Sharon (2014) studied the flow spatio-temporal organisation in a rotating turbulence generated by small jets. They claim that inertial waves might be responsible of the inverse cascade of energy. Their study is based on the observation on an inverse cascade and on several spatio-temporal spectra for different wavenumbers k showing that the energy is mainly focus on the dispersion relation of inertial waves. However the different spatio-temporal diagrams were calculated for scales smaller than the injection scale, therefore in the enstrophy cascade. Therefore, to our point of view, their data does not allow to be as affirmative as the authors and we think that the interaction between inertial waves and turbulence is still an open question.

At the view of this abundant literature it is thus legitimate to wonder if non-axisymmetric, low azimuthal wavenumber modes can arise in a rotor-stator configuration, at high Reynolds numbers, thus in the presence of a fully developed turbulence. We address here this question by performing experiments in an original device using

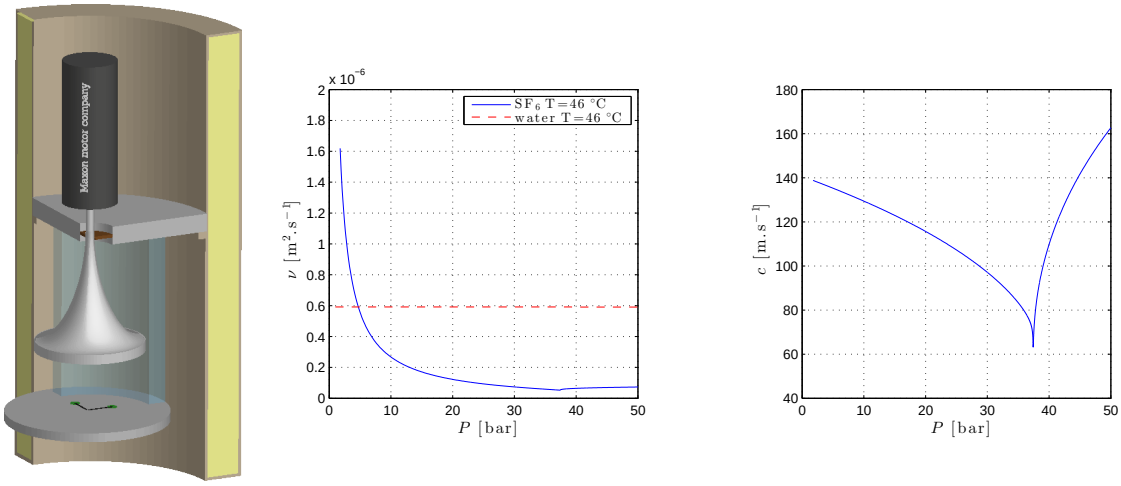

Figure 1. Left, drawing of the rotor/stator cavity with its motor, inside the thermalized pressure vessel. Center, evolution of the kinematic viscosity of the SF_6 at 46 °C as a function of the ambiant pressure P. The red line represents the kinematic viscosity of water for comparison. Right, evolution of the speed of sound of SF_6 at 46 °C as a function of the ambiant pressure. The cusp at the vicinity of the critical point is clearly visible.

sulfur hexafluoride SF_6 as working fluid at diverse temperatures and pressures. In this way, a huge range of Reynolds numbers can be explored with, as we will see, some visible compressible effects. To measure the flow characteristics, we record the pressure fluctuations on the stator for Reynolds numbers as high as $2\ 10^7$. The article is organized as follows: first our experimental set-up will be described in section 3. Then the main characteristics of turbulence and the appearance of low frequency dynamics will be described and discussed in section 4 before final conclusions will be drought in section 5.

3. Experimental setup

The flow is generated within a cylindrical enclosure consisting of a stationary shroud, two smooth rotor and stator with diameters of respectively $2R = 68$ mm and 70 mm. The outer wall is fixed to the stator as illustrated on figure 1 (left) and the rotor is driven by a brush-less electric motor which could reach an angular velocity of 10,500 rotations per minute (rpm) (i.e. a maximal rotation frequency $f_{0,max} = 175$ Hz). The interdisc spacing is $H = 40$ mm, corresponding to a heigth-to-radius aspect ratio $\gamma = 1.18$. The rotor/stator cavity with the motor is integrated into a pressurized 140 mm inner diameter cylindrical vessel (with a maximum pressure of 120 bar). The temperature control of the cavity is ensured by a thermostatically-controlled bath that regulates the entire vessel temperature through an internal circulation in the cylindrical wall of the pressurized vessel. To fill the rotor-stator cavity, gaseous SF_6 is transferred from a storage bottle and then condensed in the vessel in a 5 °C environment. Then the

pressure is gently increased to the desired working conditions by raising the temperature of the outer vessel wall. By changing the quantity of SF_6 in the vessel, different thermodynamics conditions can be chosen. The goal of this study is to describe the large scales azimuthal structures that appear on a well developed turbulence background by varying the rotational Reynolds number $Re = 2\pi\rho\mu^{-1}f_0R^2$. Measurements are performed at a rotation frequency f_0 from 17 Hz to 170 Hz, a density ρ from 6.17 kg.m^{-3} in the vapor phase to 830 kg.m^{-3} in the supercritical phase. Note however that most of the present experimental results have been obtained in the vapor phase. The SF_6 dynamic viscosity μ and the speed of sound c was determined from the temperature and the pressure measurements using the relation given in Quiñones-Cisneros et al. (2012) and the equation of state derived by Guder & Wagner (2009). The evolution of the dynamical viscosity and the speed of sound at 46 °C is presented on figure 1 center and right panel, respectively. The speed of sound of SF_6 lies between 70 and 135 m/s for the different thermodynamical conditions we have explored. Variations of these quantities allow variations of the Mach number $Ma = 2\pi Rf_0/c$ between 0.03 and 0.5 and of the Reynolds number between 5 10^4 and 2 10^7. We performed 361 runs corresponding to 17 different densities whose values can be read in the legend of figure 7.

In terms of instrumentation, three static pressure sensors are mounted flush to the stator surface and located at three different radii 10 mm, 15 mm and 20 mm from the rotation axis to determine the absolute pressure when the fluid is at rest and to characterize the distribution of the mean pressure field in the presence of a flow. Moreover, two dynamic pressure sensors are fixed on the stator at a radius of 15 mm and separated with an angle of $\pi/2$ in the azimuthal direction. These sensors have a response frequency range that extends between 0.5 Hz and 10^5 Hz. Finally, a temperature probe is placed onto the cylindrical shroud, which allows us, *a posteriori* and associated with the absolute pressure measurements, to determine the working isochores and the corresponding thermodynamical conditions. Experimentally, these conditions are reached by varying the fluid density (from higher to lower densities) by evacuating SF_6 under pressure out of the vessel. An initial measure at zero rotation rate is performed at the beginning of each experimental run in order to determine precisely the physical properties of the fluid and in particular its dynamic viscosity μ and the speed of sound c.

4. Results and discussions

4.1. Description of the spectra: cascades and mode appearance

The power spectral densities of temporal pressure fluctuations are calculated and presented for three different Reynolds numbers in the three figures 2, 3 and 4 for one of the two dynamic pressure sensors. Frequencies have been normalized by the rotating frequency f_0 as the energy is expected to be injected from the rotating disk to the fluid through the turbulent Ekman boundary layer. As can be observed, the spectra are

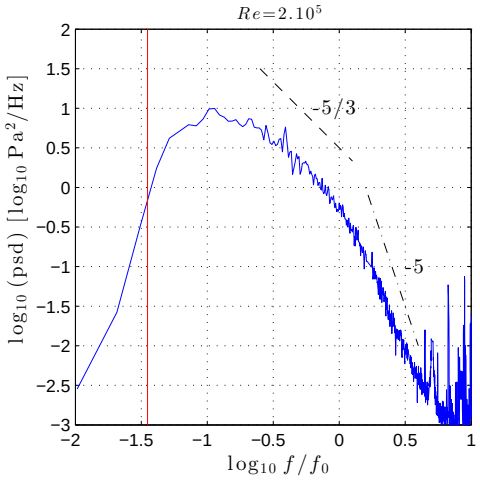

Figure 2. Example of power spectral densities for $Re = 2\ 10^5$ and $\rho = 830$ kg.m^{-3}. The inverse and the direct cascades are visible on each side of the injection frequency f_0. The red line marks the cut-off frequency of the pressure sensor high pass filter.

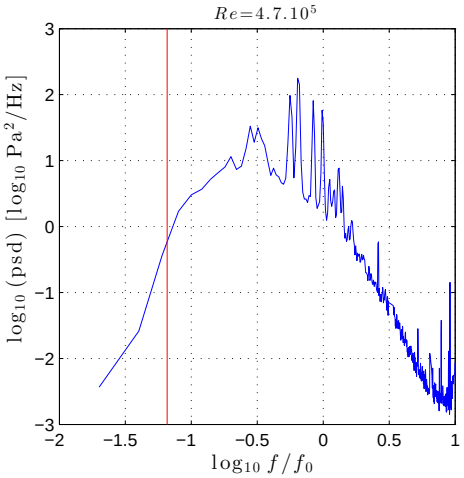

Figure 3. Example of power spectral densities for $Re = 10^6$ and $\rho = 830$ kg.m^{-3}. The inverse and the direct cascades are visible with a series of peaks superimposed on the continuous spectrum for frequencies in the range $1/4 < f/f_0 < 3/2$. The red line marks the cut-off frequency of the pressure sensor high pass filter.

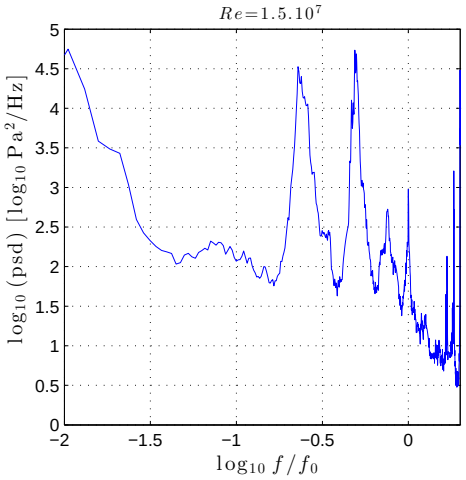

Figure 4. Example of power spectral densities for $Re = 1.5\ 10^7$ and $\rho = 830$ kg.m^{-3}. The inverse and the direct cascades are still visible, the peaks have merged and only three or four peaks are visible for frequencies $f/f_0 \approx 1, 3/4, 1/2$ and $1/4$. A very low frequency band appears at $f/f_0 \approx 10^{-2}$. The cut-off frequency of the pressure sensor high pass filter is no more visible on this plot.

divided in several frequency zones that we will describe in the following starting from the highest frequencies. For all Reynolds numbers that we have explored and for frequencies higher than f_0, a turbulent inertial cascade is observed. This part of the spectra starts at the rotor frequency f_0 and is observable up to $3f_0$. Unfortunately, because of the presence of the thick stainless steel wall of the pressurized vessel, we were not able to avoid the important electronic noise that pollutes the signals at higher frequencies. As can be observed on figures 2 and 3, the slope of this part of the spectra is very far from the -7/3 power law usually observed in classical 3D turbulence but close to -5. As described earlier, in rotating turbulence a direct enstrophy cascade is expected with a velocity spectrum proportional to k^{-3} as predicted by Kraichnan. This relation leads to a pressure spectrum proportional to k^{-5}. Therefore, using the Taylor hypothesis which assumes that small eddies are advected by the mean flow, one get a temporal spectrum for the pressure proportional to f^{-5}. Our observations are in accordance with the Kraichnan prediction for the direct cascade of enstrophy.

In addition to this cascade and starting at a Reynolds number around $\approx 10^5$, a series of frequency peaks appears in the range $1/4 < f/f_0 < 3/2$. As can be observed on figure 3, these peaks are numerous for Reynolds numbers between 10^5 and 10^6. Note that these observations can be *a priori* compared to the observations of Sørensen et al. (2009) and Sørensen et al. (2006), however we stress that here the frequency peaks grow on a fully turbulent background. When increasing the Reynolds number above 10^6, only four of these peaks are selected and remain visible at frequencies $f/f_0 \approx 1,\ 3/4,\ 1/2$

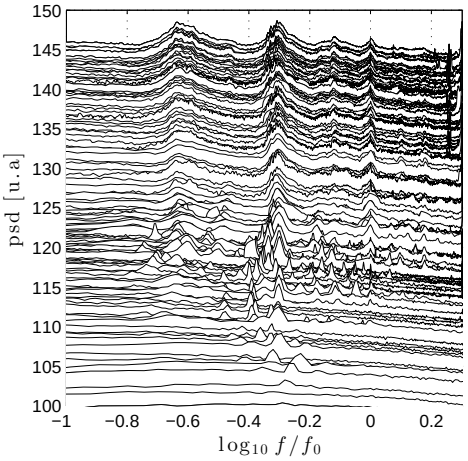

Figure 5. A global view of the spectra that shows the appearance of the peaks and their selection for a Reynolds number above 10^6. Each spectrum has been shifted vertically by $20 \log Re$ to make the pattern visible. Reynolds number varies between 10^5(bottom) and 2 10^7 (top).

and 1/4. As we will see in the following section, this low frequency dynamics can be associated to large scale azimuthal structures. One can see on figure 4 that the two most energetic peaks are located at $f_0/2$ and $f_0/4$. Figure 5 gives a synthetic view of the variations of the spectra for the whole set of Reynolds numbers. On this figure, each spectrum has been shifted vertically to make the pattern visible. The appearance, then the spreading of these peaks between $f_0/4$ and $3f_0/2$, and then the selection of the peaks for $Re \sim 10^6$ where their amplitudes increase with the Reynolds number, are particularly visible. We will focus on the description of these structures and on their evolution with the Reynolds number in subsection 4.2. Then we will present an interpretation of the growth of these modes by using a low dimensional amplitude equation model.

For frequency lower than f_0, in addition to the peaks, one can also observe a region with a slope close to $-5/3$. This low frequency part of the spectra is present in the entire range of Reynolds number and in particular for the lowest Reynolds numbers before the appearance of the peaks (see figure 2). Although we have no direct proof of it, this range of frequencies - around one tenth of the injection frequency - may correspond to an inverse cascade of energy. Indeed, if we transform the $-5/3$ exponent visible on our pressure fluctuation power spectra into the corresponding exponent for the velocity fluctuation power spectra, it becomes a $-4/3$ in complete agreement with the temporal spectra exhibited by Yarom & Sharon (2014) in a rotating turbulence experiment. According to them, this exponent might appear by the interaction between inertial waves and may correspond to an inverse cascade of energy. Here, we have no proof if there is or not a direct link between the observed peaks in the intermediate

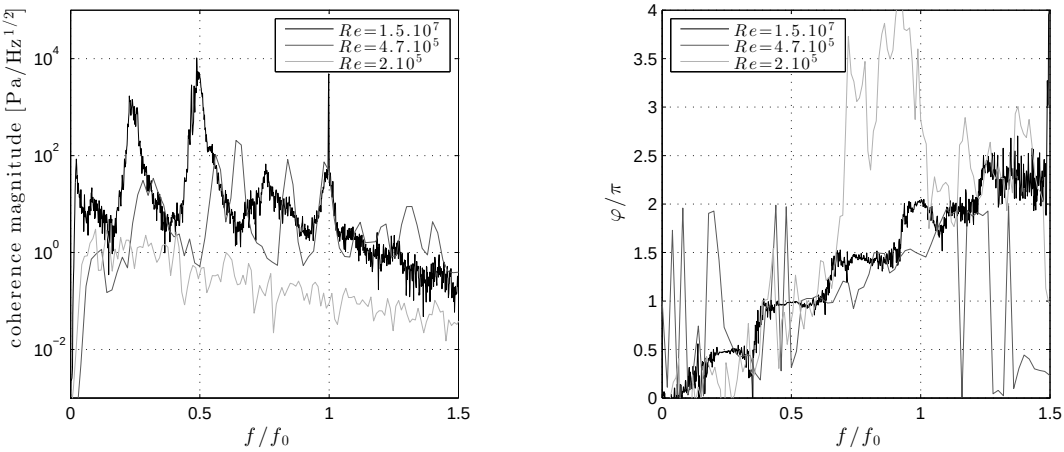

Figure 6. Evolution of the amplitude (left) and the phase (right) of the co-spectrum for the three Reynolds numbers discussed in section 4. Whereas the phase difference seems chaotic for the two lowest Re, it is well defined and exhibits plateaus at the locations of the large peaks showing the existence of large scale structures.

range of frequencies and the cascade of enstrophy or the cascade of energy. Finally, as can be observed on figure 4, at very small frequencies and although the presence of a cut-off frequency of our pressure sensors high-pass filters, we observe the appearance for the highest Reynolds number of a slow dynamics with periods as long as 100 times the disk rotation period. Note that this kind of slow dynamics has already been observed in rotating von Kármán flows (de la Torre & Burguete 2007).

4.2. Azimuthal mode dynamics

We will focus in this section on the dynamics of the hydrodynamics structures associated with the peaks observed between $f_0/4$ and f_0. To confirm the loss of axisymmetry and to understand the flow pattern, the cross power spectral densities (PSD) of the two synchronized dynamical pressure measurements have been calculated, displaying both PSDs and phase differences between both pressure sensors. By examination of the frequencies on figure 6 (left), we recognize the four peaks at the same particular values already observed on the pressure spectra. This is the proof that these structures occur indeed at large scales as they exhibit a strong coherence on the separation distance between the two pressure probes. They possess different azimuthal wave numbers m which are given by the phase difference φ between the two sensors. Indeed, as can be seen on figure 6 (right) for $f/f_0 \simeq 1/4$ a phase angle of $\pi/2$ is observed, for $f/f_0 \simeq 1/2$ it is equal to π, to $3\pi/2$ for $f/f_0 \simeq 3/4$ and to 2π for f_0. Taking into account that the sensor locations make an angle of $\pi/2$ in the azimuthal direction, leads to the determination of the lowest azimuthal wavenumbers: $m = 1,\ 2$ and 3 that correspond respectively to

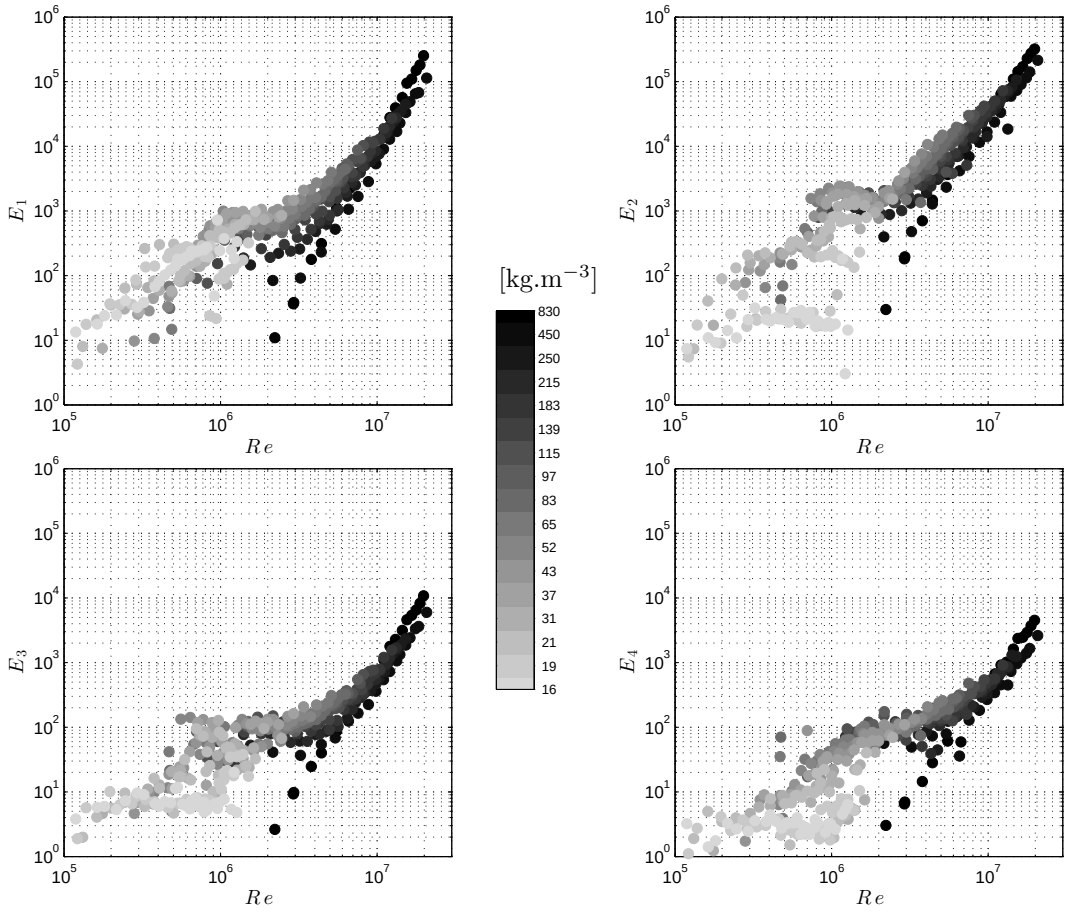

Figure 7. Evolution of the amplitude of the modes as a function of the Reynolds number Re: m =1 (top-left), m =2 (top-right), m= 3 (bottom-left), m= 4 (bottom-right). The color is coding the fluid density from 830 kg.m^{-3} (supercritical state in black) to 16 kg.m^{-3} (vapor in light gray).

frequencies $f_1/f_0 \simeq 1/4$, $f_2/f_0 \simeq 1/2$ and $f_3/f_0 \simeq 3/4$. We cannot of course distinguish between a wavenumber m and $m_p = m + 4p$, where p is an integer, due to the position of the pressure sensors.

The determination of the azimuthal wavenumber m associated with its frequencies f_m leads also to the calculation of the azimuthal phase velocity $V_{\varphi,m} = 2\pi R f_m/m$ that shows that all of these structures rotate at the same phase velocity equal to $V_{\varphi,m} = +2\pi R f_0/4$ for all m. This velocity corresponds to the half of the solid body rotation rate of the rotating core that co-rotates at half the rotating disk rate as commonly admitted for rotor/stator flows. This suggests that the excitator of these modes is spatially located into the stator boundary layer and travels at the average velocity of the rotating core and the stationary disk.

For Reynolds numbers smaller than 10^6, the numerous peaks cannot be associated to azimuthal structures due to our limited azimuthal resolution (only two probes

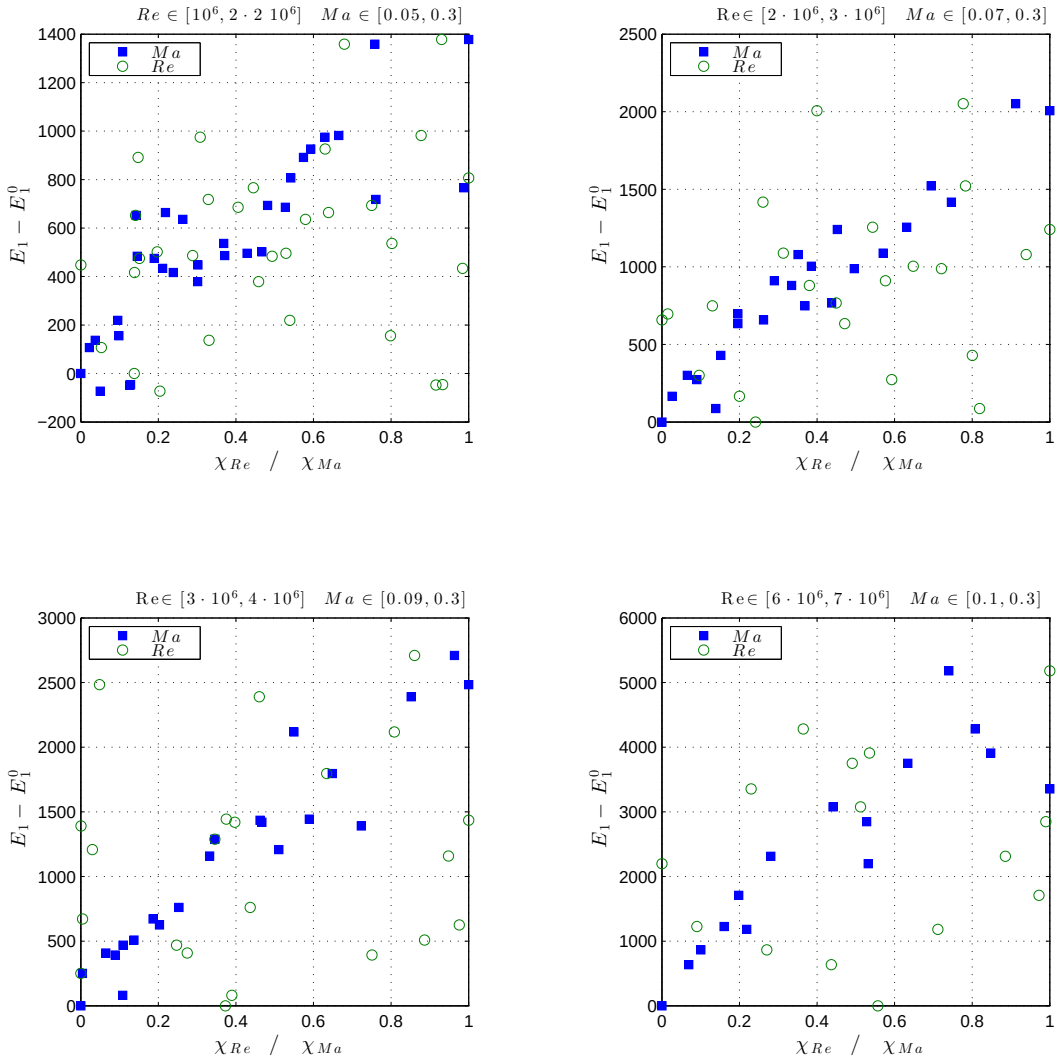

Figure 8. Evolution of the amplitude of mode $m = 1$ as a function of the normalized number χ_n. The solid blue dot represents the evolution for the normalized Mach number (χ_{Ma}) and the empty green square represents the evolution for the normalized Reynolds number (χ_{Re}), *cf.* text for details.

separated by an angle of $\pi/2$) which only allows to detect large scale structures. When the Reynolds number is increased the flow organizes itself in a particular way such that a transition occurs with a selection of a few number of modes. This threshold around 10^6 is also visible on the evolution of the energy E_m of the modes m as a function of the Reynolds number Re. At relatively low Re, one can see on figure 7 that the measurements are broadly distributed which indicates that the mode is not yet selected as we saw on figures 5 and 6. Then, for Re larger than 10^6, figure 7 shows that the experimental measurement lye on master curves with

a much weaker dispersion. This observation indicates that after the transition, the geometry of the modes and their interactions with each other are independent of the Reynolds number. We also observe that E_3 and E_4 are much smaller than E_1 and E_2. When the Reynolds number is fixed, the different experimental runs at different fluid densities differ only by the Mach number. It is thus reasonable to wonder if the dispersion of the data points depends on this number. To test this idea, we select all the experiments within a narrow window of Reynolds numbers $[Re\ ;\ Re + 10^6]$. For each of these windows, the Mach number varies typically between 0.1 and 0.3. We then define two parameters $\chi_{Re} = (Re - \min(Re))/\max(Re - \min(Re))$ and $\chi_{Ma} = (Ma - \min(Ma))/\max(Ma - \min(Ma))$ where the minimum and the maximum are determined for each window. These definitions allow us to compare on the same graph the influence of the compressibility on the amplitude of each mode. We have plotted on figure 8 the evolution of the amplitude of mode $m = 1$ as a function of these two parameters for different windows. One can see that, as expected, the evolution as a function of χ_{Re} does not show any trend but only a cloud of data points reflecting that the Reynolds number is nearly constant in the selected window. Then χ_{Re} can be seen as the experimental dispersion of the data points. On the contrary, the same data plotted as a function of the normalized Mach number χ_{Ma} clearly show that the amplitude of the mode increases quite linearly with the fluid compressibility showing that the small azimuthal wavenumber modes that we observe, are sensitive to the fluid compressibility.

4.3. Mode selection and non-linear dynamics

As it has been shown in numerical studies, inertial waves in rotor/stator cavities may be excited by the turbulent fluctuations at the boundary layer. Moreover, one can expect that at high Reynolds numbers, when viscous dissipation becomes less important, the wavelengths of these waves can be tuned within the cavity geometry and a resonance may occur. A similar phenomenon was observed in purely rotating turbulence where the inertial mode selection was due to the geometry, *cf.* Lamriben et al. (2011). In their work, turbulence was generated by a grid which excites 3 inertial modes at resonant frequencies $f_1 = 0.29 f_0$, $f_2 = 0.49 f_0$ and $f_3 = 0.74 f_0$. We observe that these frequencies are very close to our own observation. This suggests that the modes we have discovered might also be inertial modes, possibly modified by compressible effects. Further studies should be necessary to determine the exact origin of these modes.

But to go further in the characterization of the mode interactions and in the characterization of their mutual interactions, we have plotted on figure 9 the evolution of the energy E_m of modes $m = 2$, 3 and 4 as a function of energy of the mode $m = 1$, 1 and 2, respectively. One can see that as expected for lowest values, no global tendency can be defined. As already speculated, this regime corresponds to relatively low Reynolds number experiments where the frequency peaks are numerous. On the contrary, when the amplitudes increase, *i.e.* when the Reynolds number is increased above 10^6, the

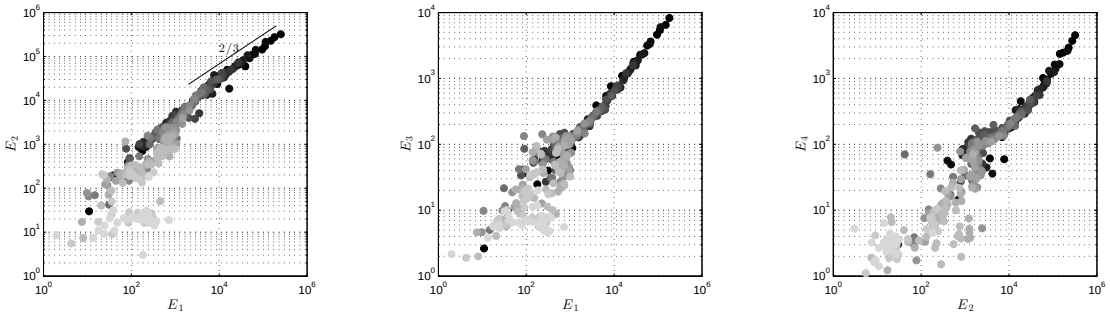

Figure 9. From left to right, evolution of the energy E_2 of mode $m = 2$ as a function of the energy E_1 of mode $m = 1$ for all the experimental runs (the 2/3 power law is a guide for the eye), of E_3 as a function of E_1 and of E_4 as a function of E_2.

flow organizes itself to reach an asymptotic regime where the amplitude E_2 is nearly proportional to $E_1^{2/3}$, E_3 to E_1 and E_4 to E_2 as can be checked on figure 9.

To describe the behavior of the different modes, we first notice that for large Re, modes $m = 3$ and $m = 4$ are slaved to respectively modes $m = 1$ and $m = 2$. Their amplitudes are much smaller and their evolution with the Reynolds number Re follows the evolution of modes $m = 1$ and $m = 2$. Therefore, the system can be reduced to the two interacting master modes $m = 1$ and $m = 2$. In order to interpret the observed scalings, we propose the following amplitude equations:

$$\begin{cases} \partial_t A_1 = \sigma A_1 - \alpha_1 A_2 \bar{A}_1 \\ \partial_t A_2 = \alpha_2 A_1^2 - \kappa A_2 - \beta A_2 |A_2|^2 \end{cases} \tag{1}$$

where the energy E_m is equal to $A_m \bar{A}_m$ where $\bar{\cdot}$ stands for the complex conjugate. Here, we assume that energy is injected from the turbulence to the modes through the linear term σA_1. Then, mode $m = 1$ saturates and feeds mode $m = 2$ through the resonant term $\alpha_1 A_2 \bar{A}_1$ with $\alpha_1 > 0$. The amplification of mode $m = 2$ is then modeled by the resonant term $\alpha_2 A_1^2$ with $\alpha_2 > 0$. Finally, we can assume that energy is dissipated through the two other contributions: κA_2 and $\beta A_2 |A_2|^2$. The first term represents the classic viscous dissipation. The second term is related to the non linear transfer of energy from the mode $m = 2$ to other modes. Note that when $\beta = 0$ the system of equations corresponds to the classical Landau model that describes the saturation of the fundamental by harmonics generation. At high Reynolds numbers, we expect that viscous dissipation is negligible compared to non linear interactions. Thus, at high Reynolds number, the stationary solution of the model given in equations (1) verifies $|A_2| \propto |A_1|^{2/3}$ and $|A_1| \propto \sigma^{3/2}$ as observed experimentally. Note that this saturation mechanism with the unexpected 2/3 exponent that does not imply viscous dissipation, should be rather general any time the energy is dissipated through non linear self-interactions. Moreover, on figure 7, we can see that at high Reynolds number Re, the amplitude of mode $m = 1$ is proportional to $Re^{3/2}$. As energy is injected by the term

σA_1, σ should then be proportional to Re which is a reasonable and simple model for the forcing.

5. Conclusion

This paper has described an experimental study of a flow confined within a smooth rotor/stator cavity with a height-to-radius aspect ratio closed to unity and using SF_6 in particular thermodynamical conditions allowing large variations of its physical properties and consequently the obtention of high Reynolds and Mach numbers. For frequencies higher than the rotation frequency of the disk f_0, an inertial cascade is observed with a slope on the spectra very close to -5. This -5 slope for the pressure fluctuation spectrum corresponds to the -3 exponent of the velocity fluctuation power spectra as predicted by Kraichnan (1967) for the 2D turbulence direct enstrophy cascade. For small frequencies, we have also detected on the pressure temporal spectra a $-5/3$ slope region which may correspond to an inverse cascade of energy. Starting at a Reynolds number around 10^5 and in addition to the cascades, a series of peaks appears at frequencies in the range $1/4 < f/f_0 < 3/2$. They imply that non axisymmetric oscillating coherent structures come into play and lead to a complex flow topology. Whereas these peaks are numerous for Reynolds numbers in the range $10^5 < Re < 10^6$, when increasing the Reynolds number above 10^6, only three of them are selected at frequencies $f/f_0 \approx 1/4, 1/2$ and $3/4$. The study of the phase difference between two pressure probes shows that these peaks correspond to modes with azimuthal wavenumbers $m = 1, 2$ and 3 respectively. The appearance of these modes at very high Reynolds numbers can then be interpreted as the response to a turbulent forcing coming from the stator boundary layer. Although we have no proof of it, we suspect these modes to be inertial modes, possibly modified by compressible effects as their amplitude depends on the Mach number. Finally their scaling behavior has been interpreted with a low dimensional amplitude equations. Therefore, our experiments on rotor-stator cavity flows at very high Reynolds number demonstrate that large scale structures are not destroyed by turbulence. On the contrary, we show that they are fed by turbulence and then can even grow and survive superimposed on inertial turbulent cascades.

Acknowledgments

This work has been carried out in the framework of the Labex MEC Project (No. ANR-10-LABX-0092) and of the A*MIDEX Project (No. ANR-11-IDEX-0001-02), funded by the "Investissements d'Avenir" French Government program managed by the French National Research Agency (ANR).

References

Barbosa E 2002 Etude numérique des écoulements tridimensionnels dans des cuves cylindriques rotor-stator PhD thesis Université d'Evry Val-d'Essone.

Baroud C N, Plapp B B, She Z S & Swinney H L 2003 *Phys. Fluids* **15**, 2091.

Blackburn H & Lopez J 2002 *J. Fluid Mech.* **465**, 33–58.

Czarny O, Iacovides H & Launder B 2002 *Flow, Turb. and Comb.* **69**, 51–61.

de la Torre A & Burguete J 2007 *Phys. Rev. Lett.* **99**, 054101.

Escudier M 1984 *Exp. Fluids* **2**, 189–196.

Gauthier G, Gondret P, Moisy F & Rabaud M 2002 *J. Fluid Mech.* **473**, 1–21.

Gelfgat A Y 2015 *Fluid Dyn. Res.* **47**, 035502.

Gelfgat A Y, Bar-Yoseph P Z & Solan A 1996 *J. Fluid Mech.* **311**, 1–36.

Gelfgat A Y, Bar-Yoseph P Z & Solan A 2001 *J. Fluid Mech.* **438**, 363–377.

Guder C & Wagner W 2009 *J. Phys. Chem. Ref. Data* **38**(1), 33–94.

Gutierrez-Castillo P & Lopez J 2015 *Eur. J. Mech B/Fluids* **52**, 76–84.

Hart J & Kittelman S 1996 *Phys. Fluids* **8**, 692.

Jacques R, Daube O & Le Quéré P 2002 *Int. J. Heat Fluid Flow* **23**, 381–397.

Kraichnan R 1967 *Phys. Fluids* **10**, 1417–1423.

Lamriben C, Cortet P P, Moisy F & Maas L R M 2011 *Phys. Fluids* **23**, 015102.

Launder B, Poncet S & Serre E 2010 *Annu. Rev. Fluid Mech.* **42**, 229–248.

Lopez J 2006 *J. Fluid Mech.* **553**, 323–346.

Lopez J 2012 *Phys. Fluids* **24**, 014101.

Lopez J, Hart J, Marques F, Kittelman S & Shen J 2002 *J. Fluid Mech.* **462**, 383–409.

Lopez J M 1990 *J. Fluid Mech.* **221**, 533–552.

Lopez J M 1998 *J. Fluid Mech.* **359**, 49–79.

Lopez J M, Marques F & Sanchez J 2001 *J. Fluid Mech.* **439**, 109–129.

Lopez J & Marques F 2010 *Phys. Fluids* **22**, 114109.

Lopez J & Marques F 2014 *Phys. Rev. E* **89**, 013013.

Lopez J, Marques F, Rubio A & Avila M 2009 *Phys. Fluids* **21**, 114107.

Marques F & Lopez J M 2001 *Phys. Fluids* **13**, 1679.

Poncet S, Chauve M & Le Gal P 2005 *J. Fluid Mech.* **522**, 253–262.

Poncet S, Serre E & Launder B 2009 Three-dimensionnal unsteady large-scale vortical structures embedded in turbulent rotor-stator flow. unpublished: https://www.researchgate.net/publication/259006774.

Quiñones-Cisneros S E, Huber M L & Deiters U K 2012 *J. Phys. Chem. Ref. Data* **41**(2), 023102.

Schouveiler L, Le Gal P & Chauve M 1998 *Phys. Fluids* **10 (11)**, 2695–2697.

Schouveiler L, Le Gal P & Chauve M 2001 *J. Fluid Mech.* **443**, 329–350.

Sørensen J, Gelfgat A, Naumov I & Mikkelsen R 2009 *Phys. Fluids* **21**(5), 054102.

Sørensen J, Naumov I & Mikkelsen R 2006 *Exp. Fluids* **41**(3), 425–440.

Sotiropoulos F & Ventikos Y 2001 *J. Fluid Mech.* **426**, 155– 175.

Stevens J L, Lopez J M & Cantwell B J 1999 *J. Fluid Mech.* **389**, 101–118.

Yarom E & Sharon E 2014 *Nature Phys.* **10**, 510–514.